Author/s:
OwYong, TC;Ding, S;Wu, N;Fellowes, T;Chen, S;White, JM;Wong, WWH;Hong, Y

Title:
Optimising molecular rotors to AIE fluorophores for mitochondria uptake and retention

Date:
2020-12-07

Citation:
OwYong, T. C., Ding, S., Wu, N., Fellowes, T., Chen, S., White, J. M., Wong, W. W. H. & Hong, Y. (2020). Optimising molecular rotors to AIE fluorophores for mitochondria uptake and retention. CHEMICAL COMMUNICATIONS, 56 (94), pp.14853-14856. https://doi.org/10.1039/d0cc06411d.

Persistent Link:
https://hdl.handle.net/11343/285513

Optimizing Molecular Rotors to AIE Fluorophores for Enhanced Mitochondria Uptake and Retention

Tze Cin Owyong,[a,b] Siyang Ding,[b] Na Wu,[a] Thomas Fellowes,[a] Jonathan M. White,[a] Wallace W. H. Wong,*[a] and Yuning Hong*[b]

Dedication ((optional))

[a] T. C. Owyong, N. Wu, T. Fellowes, Prof., J. M. Whites, Dr., W. W. H. Wong
ARC Centre of Excellence in Exciton Science, School of Chemistry, Bio21 Institute, The University of Melbourne, Parkville, VIC 3010 Australia
E-mail: wwhwong@unimelb.edu.au
[b] S. Ding, Dr., Y. Hong
Department of Chemistry and Physics, La Trobe Institute for Molecular Science, La Trobe University, Melbourne, VIC 3086, Australia
E-mail: Y.Hong@latrobe.edu.au

Supporting information for this article is given via a link at the end of the document.

Abstract: Molecular rotors exhibit fluorescence enhancement in a confined environment and thus have been used for biological imaging especially in monitoring intracellular viscosity. However, conventional molecular rotors could suffer from self-aggregation caused quenching. In this work, we report the synthesis of a series of red emissive fluorescent molecular rotors based on cationic α-cyanostilbene with and without profound aggregation-induced emission (AIE) characteristics. With excellent specificity to stain mitochondria, we further demonstrate the alternation of substituents on the pyridinium of the dyes to influence on cell uptake and retention upon fixation.

Introduction

Fluorescent molecules have been shown to be powerful and crucial tools in many fields with biology being one of them. A class of fluorophores that have been well used are the molecular rotors.[1-2] The general structure of these fluorophores are conjugated molecules containing a structure that can rotate relative to the whole molecule. When free intramolecular rotation of the dye occurs, a dye excited by light can undergo relaxation to the ground state through non-radiative pathways, and thus there is low fluorescence intensity and short fluorescence lifetime. Upon restriction of intramolecular rotation (RIR), by viscosity or steric effects, the nonradiative pathways are inhibited and thus results in an enhancement of fluorescence intensity and a prolonged fluorescence lifetime.[3] Aggregation induced emission (AIE) active molecules have similar feature to fluorescent molecular rotors. A key difference, between conventional fluorescent molecular rotors is that in conditions where the local dye concentration is high, conventional molecular rotors can undergo energy transfer, which leads to quenching effects. AIE-active molecules, due to their chemical structure, have greater difficulties packing closely or engage in π-π stacking interactions, and thus exhibit strong fluorescence at high concentration or in aggregate states.[4-5]

In this work, we report the synthesis and study of a cationic α-cyanostilbene, namely **ASC**, the reported compound **ASCP**, and its new derivatives.[6] All these molecules possess molecular rotor type of photophysical behaviour. While **ASC** is non-AIE active, addition of a phenyl ring bridge endows the AIE property to the **ASCP** series. With large Stokes shift and emission in the red region, we further explore the application of **ASCP** series for mitochondrial imaging in cells.

As key organelle in eukaryotic cells, mitochondria involve in production of ATP, the currency of energy in cells.[7] Apart from the crucial process of providing energy, mitochondria are involved with reactive oxygen species (ROS), participate in transcription regulation and govern cell death.[8-10] Furthermore, the dynamics and morphology of mitochondria also has been implicated in disease and affected by a set of proteins, with mutations leading to neurodegenerative diseases, such as Parkinson's and Huntington's disease.[11-12] Further development and improving upon current fluorescent mitochondria stains would give insight for monitoring these processes.

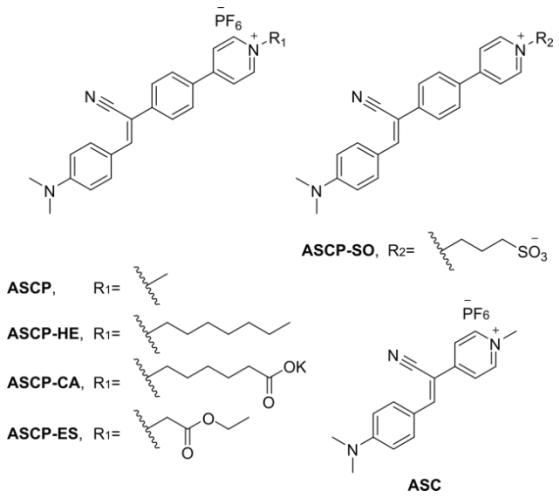

Figure 1. Chemical structures of dyes in this study.

In many biological applications, real-time monitoring of mitochondria morphological changes is of great interest. On the other hand, fixation by aldehyde of the cells is commonly used for the ease of sample handling and preservation as well as for further antibody labelling for recognition of a particular protein.

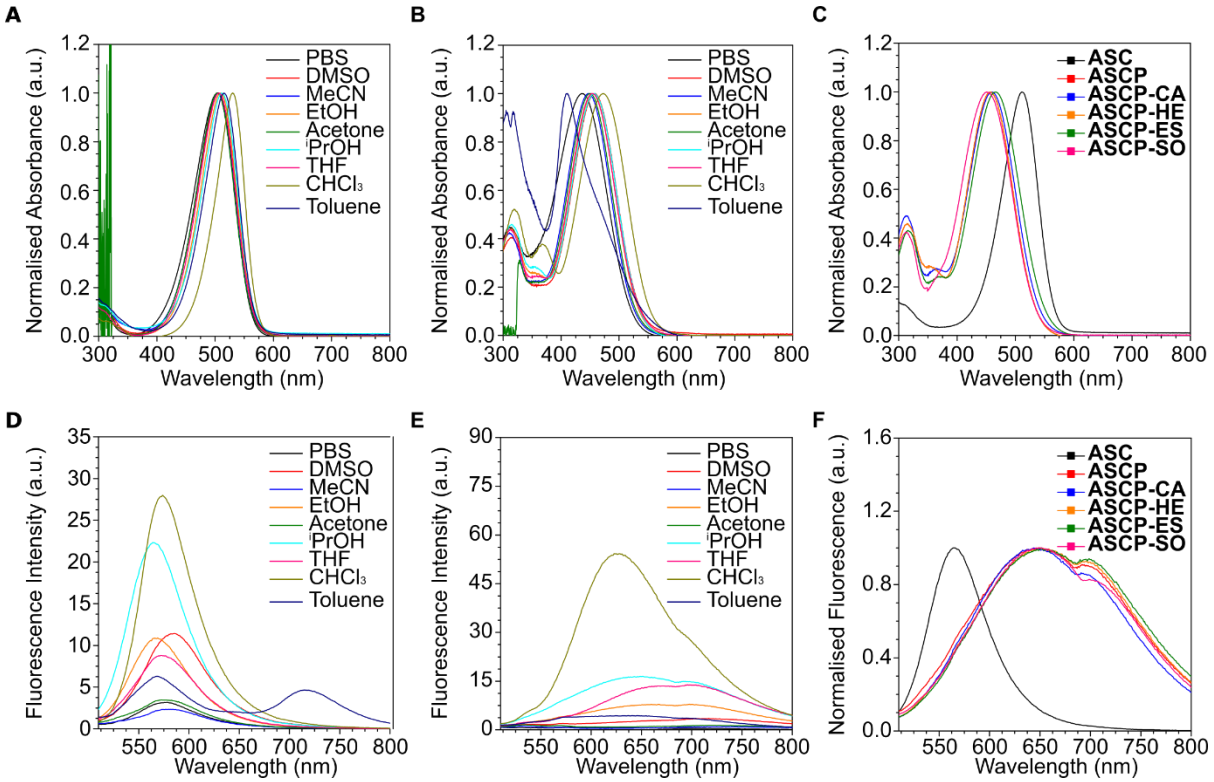

Figure 1. Absorbance and fluorescence emission spectra for **ASC** and **ASCP** and derivatives. (A-C) Normalized UV-vis absorption spectra of (A) **ASC** and (B**) ASCP** in different solvents. (C**)** Comparison of absorption spectra of all dyes measured in ^{i}PrOH. (D-F) Fluorescence spectra of (D) **ASC** and (E) **ASCP** in different solvents. (F) Comparison of emission spectra of dyes measured in ^{i}PrOH. PBS was Na_2HPO_4 at 20 mM concentration. 488 nm excitation wavelength was used for fluorescence measurements. 10 µM dye concentration was used for all measurements.

Although many of these stains work in the live cell conditions, retention of their signal after fixation is usually achieved by using covalent strategy as seen in the commercial MitoTracker dyes. Covalent labelling, however, could, potentially affect the dynamics when used in live cells. In this work, we demonstrate that molecular structure plays a large role in cellular uptake and retention. By altering the substituent on the pyridinium moiety, we improve the cell uptake and retention of **ASCP**, demonstrating a noncovalent strategy for labelling mitochondria in both fixed and live cells.

Results and Discussion

Dye Synthesis

The synthetic routes to **ASC** and **ASCP** and derivatives are shown in Scheme S1-3 in the supporting information. In short, for ASCP and derivatives, a Knoevenagel condensation reaction between 4-dimethylaminobenzaldehyde and 4-bromophenylacetonitrile gave the electron donor-acceptor cores of interest. A palladium catalysed Suzuki cross-coupling was used to install 4-pyridylboronic acid onto the fluorophore core. Alkylation of the pyridine took place using respective alkylative reagents, before anion exchange reactions to obtain the final products using potassium hexafluorophosphate. For **ASC**, a Knoevenagel condensation reaction between 4-dimethylaminobenzaldehyde and 4-pyridylacetonitrile hydrochloride gave the electron donor-acceptor cores of interest. Alkylation of the pyridine took place using iodomethane, before anion exchange reaction to obtain the final products using potassium hexafluorophosphate. All synthesised products were characterized by ^{1}H, ^{13}C NMR and high-resolution mass spectrometry (refer to SI). The structures of **ASC** and **ASCP** were further confirmed by single crystal X-ray crystallography (Figure S1, Table S1-2).

Photophysical Characterization

The UV-vis absorption spectra of **ASC** and **ASCP** in different solvents were measured first. The results showed that the smaller **ASC** has an absorption maximum ranging from 504–530 nm and exhibits minimal shifts with regards to solvent dielectric constants (Figure 2A). On the other hand, **ASCP** has an absorbance maximum in the range of 411–497 nm and a red shift in the absorbance maximum in less polar, lower dielectric constant solvent (Figure 2B, Table S3). The **ASCP** derivatives have very similar absorption characteristics as **ASCP** (Figure 2C, S2).

The fluorescence emission spectra showed that **ASC** emits mainly at around 560 nm in various solvents with minimal changes in the wavelength with some differences in fluorescence intensity (Figure 2D). The only exception was in toluene where a second emission peak at around 715 nm was observed. A plausible explanation for this spectra character is the formation of excimers when dye molecules self-aggregate in toluene. For **ASCP** and derivatives, we observed red-shifted spectra in a more polar, higher dielectric constant solvent (like DMSO), as compared to nonpolar solvents such as chloroform (Figure 2E and Figure S3). The largest fluorescence intensity came from chloroform, and we attributed this to dye self-aggregation and subsequent AIE affects (vide infra Figure 3B). While the main emission peaks of **ASCP**

A

Photoluminescent Quantum Yield (PLQY)	Mean
ASC	6.8%
ASCP	18.5%
ASCP-CA	23.2%
ASCP-HE	22.4%
ASCP-ES	20.7%

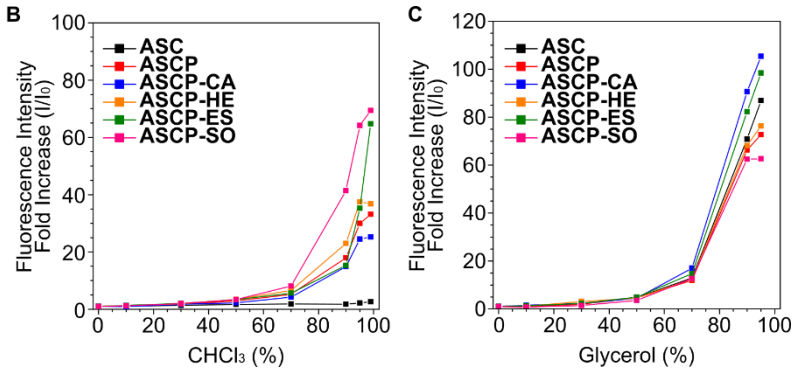

Figure 2. Fluorescence response upon rigidification. (A) Absolute photoluminescent quantum yield (PLQY) of dyes in PMMA matrix (2% weight ratio). Note that due to the poor solubility of **ASCP-SO** in acetone, its PLQY was not measured. (B) Fold of increase in fluorescence intensity of dyes in DMSO and chloroform ($CHCl_3$) mixtures with increasing fraction of $CHCl_3$ from 0, 10, 30, 50, 70, 90, 95, and 99 vol%. (C) Fold of increase in fluorescence intensity of dyes in water and glycerol mixtures with increasing fraction of glycerol from 0, 10, 30, 50, 70, 90, 95 vol%. Plots were obtained by taking fluorescence emission intensity value at 575 nm for **ASC** and 650 nm for **ASCP** derivatives. 10 μM dye concentration was used for dye self-aggregate and viscosity experiments. 488 nm excitation wavelength was used for all measurements.

and derivates are red-shifted to around 650 nm, their emission spectra are also broad compared to **ASC** (Figure 2F). When comparing the Stokes shift of the dyes, ASC possesses a much smaller Stokes shift (53 nm) in comparison to **ASCP** derivatives with Stokes shift in the range of 170–195 nm (Table S4).

From the absorption spectra in Figure 2C, we can estimate that **ASC** has a better π conjugation than **ASCP** and derivatives. The X-ray crystallography data further confirmed that **ASC** has a more planar conformation than **ASCP**, with smaller torsional angles between the aromatic rings and the central double bond (Figure S4). The larger conjugation could potentially confine the conformation to a larger extent as seen in the smaller Stokes shift and narrower absorption and emission peaks observed in **ASC** compared to those of **ASCP** (Table S4 and Figure 2C,F).[5] DFT calculations showed a clearer distinction of the HOMO and LUMO electron density distributions of **ASCP** with HOMO most localizing on the electron donor dimethylamine moiety while the LUMO was more centred on the positively charged electron withdrawing pyridinium (Figure S5). In the case of **ASC**, similar HOMO and LUMO distributions were found but less distinguishable. This is consistent with our observation that the fluorescence of **ASC** is less sensitive to solvent polarity than that of **ASCP** (Figure 2D,E). The electrostatic potential data from X-ray diffraction experiment further supported this observation of HOMO-LUMO distribution for **ASC** (Figure S6).

Molecular Rotor *versus* AIE

We then proceeded to further characterize the molecular rotor and AIE nature of the dyes. To determine the quantum yield of individual molecules undergoing restriction of intramolecular rotations, absolute photoluminescence quantum yields (PLQY) were measured in thin films with 2% dye doping in poly(methyl methacrylate) (PMMA). We found that the **ASCP** series have higher PLQY, in the range of 15 – 23%, while the PLQY of **ASC** was recorded at 7% (Figure 3A, Table S5).

To study the self-aggregation effect on fluorescence, we measured the fluorescence intensity of dyes in DMSO/chloroform ($CHCl_3$) with increased fraction of chloroform, a poor solvent for the dyes. We observed that for the **ASCP** series, there were large fluorescence intensity enhancements beyond 70% chloroform. Most **ASCP** dyes achieved maximum fluorescence intensity at 99% chloroform with fluorescence fold increases ranging from 25–82 folds. For the smaller **ASC**, we only observed minimal increase in fluorescence intensity at 99% chloroform with modest 2.6 fold increase (Figure 3B, S7). This result demonstrated a stronger AIE characteristics in **ASCP** compared to **ASC**.

To induce restriction of intramolecular motions, we then measured the viscosity effect by increasing glycerol percentage. Our results showed that above 50% glycerol concentration, all dyes had an increases of fluorescence intensity. Maximum dye intensity was observed at the highest glycerol condition measured (95%) (Figure 3C, S8). These results showed that all dyes possess molecular rotor behavior, where rigidification of the molecule results in the fluorescence intensity enhancement.

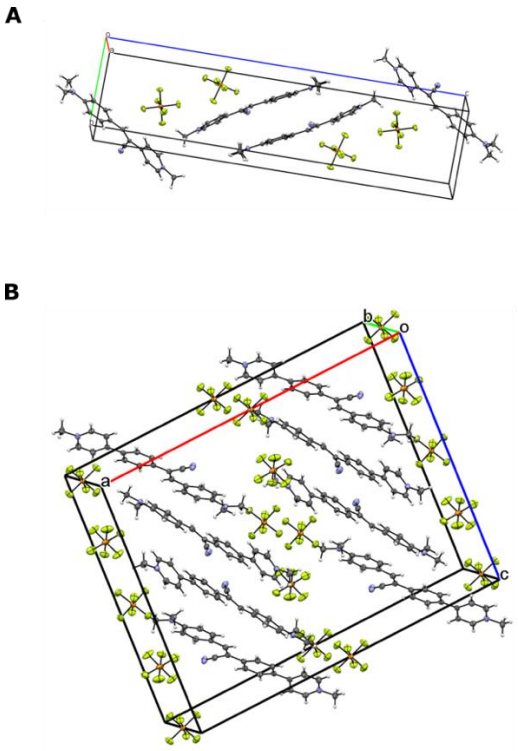

Figure 3. Molecular packing of (A) **ASC** and (B) **ASCP** acquired from X-ray crystallography data.

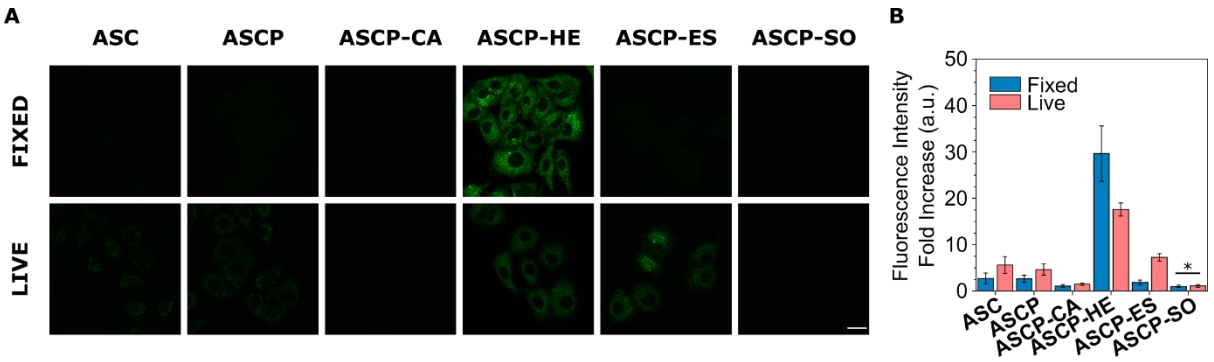

Figure 4. Comparison of dye cell uptake and retention. (A) Confocal images of dye staining A549 cells with (fixed) and without fixation (live). (B) Fluorescence intensity analysis of imaged cells. Unless specified in the figure, comparison between respective fixed and live fluorescence intensities for each respective dye had $p < 0.0001$ significance. *= $p < 0.05$. mean ± sd. Scale Bar, 20μm. For **ASCP** and derivatives (excitation: 488 nm; emission: 615–650 nm), **ASC** (excitation: 488 nm; emission 520–560 nm).

An explanation of this improved AIE property in **ASCP** could be seen from the crystal packing from X-ray diffraction data (Figure 4). Both **ASC** and **ASCP** have a head-to-tail crystal packing structure (Figure 4). Closer inspection of the intramolecular torsion angles revealed that the fluorophore cores of **ASC** and **ASCP** both had small torsion angles ranging from 1.58–5.96° between aryl groups and the central double bond. The pyridinium group off the **ASCP** fluorophore, however, was observed to be more twisted and had a larger torsion angle of 17.5 (Figure S4). This twisted ring could have increased resistance of the molecule to pack tightly and could have given rise to the addition AIE characteristics seen in the high PLQY in solid film and the larger fluorescence enhancement in the aggregate state.

Substituent Effect on Cell Uptake and Retention

For our cell experiments, we evaluated the cytotoxicity of the dyes by using AlamarBlue™ cell viability kit. All dyes measured did not have a significant adverse effect on cell viability even after treatment of 24 h, demonstrating minimal cytotoxicity and excellent compatibility with cells (Figure S9). Our first attempt of cell staining was conducted on staining live A549 cells with the dyes at the desired concentration followed by fixation with 4% paraformaldehyde (PFA). Confocal imaging shown that among **ASC** and **ASCP** and derivatives, only **ASCP-HE** with a hexyl chain showed strong fluorescence staining, mitochondria-like pattern in the cells under 488 nm laser excitation (Figure 5A).

In order to determine the reasons for the lack of staining for most of the dyes, live cell imaging without PFA fixation was carried out with the same imaging conditions (Figure 5A). While **ASCP-HE** and **ASCP-ES** gave the highest fluorescence intensity in the live cells, the response for **ASC**, **ASCP** and **ASCP-ES** was improved, and mitochondria-like staining patterns were also observed. In the case of **ASCP-HE**, we observed good staining with appreciable intensity in both live and fixed cells. For zwitterionic **ASCP-CA** and **ASCP-SO**, minimal cell uptake was observed in either live or fixed conditions.

Further analysis of the fluorescence intensity of stained compartments yielded interesting results and provided some explanation to the differing staining efficiency in fixed and live cells (Figure 5B). **ASC**, **ASCP** and **ASCP-ES** all had higher fluorescence intensities in live cells, implying that fixation of the cells affects the retention of the dyes. These results suggested that a net positive charge would assist in membrane permeability and thus increase the cell uptake of the dye. Meanwhile, fluorophore lipophilicity plays an important role in not only cell uptake but also retaining the non-covalent dye molecules in the cells, as seen in **ASCP-HE** with a hydrophobic non-charged hexyl chain. Therefore, the lack of staining for the dyes except **ASCP-HE** in fixed cells could arise from two reasons, or a combination of both. The first was the lack of penetration of dye before fixation. The second, was low retention of dye in cells upon fixation.

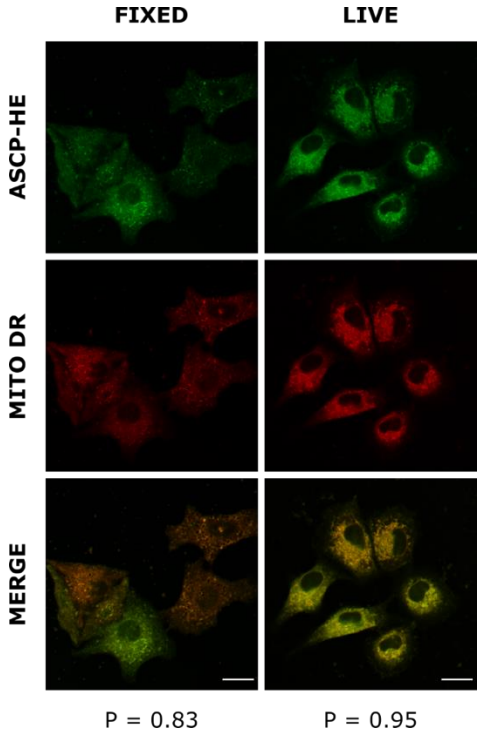

Figure 5. Confocal microscopy images of intracellular distribution of **ASCP-HE** stained A549 cells with (fixed) and without fixation (live). A549 cells were stained with **ASCP-HE** and counterstained with MitoTracker™ Deep Red FM (**MITO DR**) for visualisation of mitochondria. Pearson correlation values (P) were calculated. Cells were stained using 5 μM of **ASCP-HE** and 500nM **MITO DR**. Scale Bar, 20μm. For **ASCP-HE** (excitation: 488 nm; emission: 615–650 nm), **MITO DR** (excitation: 633 nm; emission 660–700 nm).

With the promising results from **ASCP-HE**, we carried out co-localization experiments to confirm the staining patterns. Dye crosstalk experiments verified that there was no bleed-through

from the mitochondria stain, MitoTracker™ Deep Red (**MITO DR**) in our dye channel (Figure S10). Although **ASCP-HE** emits in the red region (signal collected 615–650 nm), to differentiate from **MITO DR**, we used pseudo green color to represent **ASCP-HE** signals and red for **MITO DR**. The staining patterns for **ASCP-HE** were colocalized with **MITO DR**, with Pearson correlation factor (P) of 0.83 (Figure 6). **ASCP-HE** was further confirmed to localize in fixed cells by obtaining z-stack images (Figure S11). Subsequent live cell colocalization experiments were then carried out, which showed the staining patterns of **ASCP-HE** was greatly colocalized with **MITO DR** with P of 0.95 (Figure 6).

Conclusion

In summary, we have designed and synthesized a series of cationic α-cyanostilbene derivatives, including **ASC**, **ASCP** and its derivatives. By comparing the photophysical behaviour of **ASC** and **ASCP**, we demonstrated the correlation between the extent of conjugation and structure rigidity. We further studied their fluorescence response upon rigidification in solid film, upon aggregation and in high viscosity. Whereas all of the molecules possess molecular rotor like behaviour, the addition of a phenyl bridge to **ASC** leads to a remarkable enhancement of the AIE effect. These red-emitting dyes show specificity to mitochondria. Upon changing the substituent on the pyridinium of **ASCP**, we demonstrated the crucial role of lipophilicity in cell uptake and developed a simple, non-covalent strategy to achieve excellent retention upon cell fixation. Such strategy could be further applied in other organelle targeting agents.

Experimental Section

Materials

1-Bromohexane, 6-bromohexanoic acid, 4-bromophenyl acetonitrile, ethyl bromoacetate, iodomethane, 1,3-propanesultone, 4-pyridylacetonitrile hydrochloride, tricyclohexylphosphine tetrafluoroborate, tris(dibenzylideneacetone)dipalladium(0) were obtained from Sigma Aldrich. 4-pyridylboronic acid was obtained from Boron Molecular. Potassium hydroxide and potassium phosphate tribasic were obtained from Chem-supply. 4-Dimethylaminobenzaldehyde, potassium hexafluorophosphate, were obtained from AK Scientific. Anhydrous solvents were dried by molecular sieves (4Å). Hexanes refer to the fraction of boiling point range 40-60ºC. For biological experiments, materials were obtained from Sigma Aldrich or Thermo Scientific. MitoTracker™ Deep Red were obtained from Thermofisher Scientific.

Synthesis

Detailed synthesis scheme for all intermediates and products is given in the Supporting Information (Scheme S1-S3). Flash chromatography was carried out on silica gel (Merck Kieselgel 60 (230 – 400 mesh)) under pressure of nitrogen.

(Z)-2-(4-bromophenyl)-3-(4-(dimethylamino)phenyl)acrylonitrile (3): 4-Bromophenylacetonitrile (8.77 g, 45.0 mmol) and 4-dimethylaminobenzaldehyde (7.45 g, 50.0 mmol) was added with potassium hydroxide (3.40 g, 55.0 mmol) in 100 mL of ethanol and stirred at room temperature for 16 h. Upon completion of reaction, the yellow precipitates were filtered, washed with ethanol and dried under reduced pressure to yield the product as a yellow coloured solid in 96% yield (14.1 g). ^{1}H NMR (400 MHz, $CDCl_3$) δ 7.84 (d, *J* = 9.0 Hz, 2H), 7.50 (q, *J* = 8.8 Hz, 4H), 7.37 (s, 1H), 6.71 (d, *J* = 8.9 Hz, 2H), 3.06 (s, 6H). ^{13}C NMR (100 MHz, $CDCl_3$) δ 151.79, 142.79, 134.58, 131.93, 131.40, 126.87, 121.79, 121.23, 119.08, 111.56, 103.13, 40.00. HRMS (ESI+): *m*/*z*. 327.04925 [$C_{17}H_{16}N_2Br$ $(M+H)^+$, calcd 327.04914].

(Z)-3-(4-(dimethylamino)phenyl)-2-(4-(pyridin-4-yl)phenyl)acrylonitrile (2): 3 (8.15 g, 25 mmol) was added to 4-pyridineboronic acid (3.38 g, 27.5 mmol), $Pd_2(dba)_3$ (220 mg, 0.25 mmol), $P(Cy)_3{\cdot}HBF_4$ (221 mg, 0.60 mmol), K_3PO_4 (13.3 g, 62.5 mmol) and placed under N_2. An N_2 sparged solution of dioxane (70 mL) and H_2O (34 mL) was then added to the reaction mixture, stirred and refluxed for 24 h. Upon completion, the reaction mixture was cooled and extracted with DCM (3 x) and washed with water (3 x). The organic layer was then dried over magnesium sulfate, filtered and concentrated. The crude product was then purified by column chromatography (99:1 to 9:1 DCM: EtOAc) to obtain the pure product as an orange solid in 73% yield (5.92 g). ^{1}H NMR (400 MHz, $CDCl_3$) δ 8.68 (d, *J* = 6.0 Hz, 2H), 7.89 (d, *J* = 8.9 Hz, 2H), 7.72 (m, 4H), 7.53 (d, *J* = 6.0 Hz, 2H), 7.48 (s, 1H), 6.74 (d, *J* = 8.9 Hz, 2H), 3.08 (s, 6H). ^{13}C NMR (100 MHz, $CDCl_3$) δ 151.86, 150.36, 147.31, 142.96, 137.38, 136.42, 131.52, 127.40, 126.02, 121.32, 119.24, 111.61, 103.44, 40.04. HRMS (ESI+): *m*/*z*. 327.16637 [$C_{22}H_{20}N_3$ $(M+H)^+$, calcd 326.16517].

(ASCP): Compound **2** (200 mg, 0.614 mmol) was added to MeCN (10 mL). Iodomethane (131 mg, 0.912 mmol) was then added to the reaction mixture, stirred and refluxed for 24 h. Upon completion of the reaction, the reaction mixture was cooled to room temperature, precipitated with Et_2O, filtered and washed with Et_2O. The precipitate was then redissolved in acetone (20 mL) and saturated KPF_6 aqueous solution (20 mL) and stirred for 1 h. Acetone was then removed and the precipitate was filtered and washed with water to obtain the pure product as a red solid in 75% yield (224 mg). ^{1}H NMR (400 MHz, DMSO) δ 9.00 (d, *J* = 6.7 Hz, 2H), 8.54 (d, *J* = 6.7 Hz, 2H), 8.19 (d, *J* = 8.6 Hz, 2H), 8.06 (s, 1H), 7.94 (m, 4H), 6.85 (d, *J* = 9.0 Hz, 2H), 4.32 (s, 1H), 3.06 (s, 3H), 2.50 (s, 6H). ^{13}C NMR (100 MHz, DMSO) δ 153.59, 152.59, 145.99, 145.07, 139.02, 132.66, 132.19, 131.06, 129.37, 129.18, 127.49, 126.24, 124.61, 124.14, 121.84, 120.96, 119.48, 112.09, 101.00, 56.84, 47.46, 40.04. HRMS (ESI+): *m*/*z*. 340.18026 [$C_{23}H_{22}N$ $(M-PF_6)^+$, calcd 340.18082].

(ASCP-CA): Compound **2** (100 mg, 0.307 mmol) was added to MeCN (5 mL). 6-bromohexanoic acid (599 mg, 3.07 mmol) was then added to the reaction mixture, stirred and refluxed for 24 h. Upon completion of the reaction, the reaction mixture was cooled to room temperature, precipitated with Et_2O, filtered and washed with Et_2O. The precipitate was then redissolved in acetone (10 mL) and saturated KPF_6 aqueous solution (10 mL) and stirred for 1 h. Acetone was then removed and the precipitate was filtered and washed with water to obtain the pure product as a red solid in 48% yield (92.3 mg). ^{1}H NMR (400 MHz, DMSO) δ 12.02 (s, 1H), 9.08 (d, *J* = 6.6 Hz, 2H), 8.55 (d, *J* = 6.6 Hz, 2H), 8.19 (d, *J* = 8.5 Hz, 2H), 8.04 (s, 1H), 7.92 (m, 4H), 6.83 (d, *J* = 8.9 Hz, 2H), 4.55 (t, *J* = 7.3 Hz, 2H), 3.04 (s, 6H), 2.22 (t, *J* = 7.2 Hz, 2H), 2.01 – 1.86 (m, 2H), 1.65 – 1.48 (m, 2H), 1.31 (m, 2H). ^{13}C NMR (100 MHz, DMSO) δ 174.75, 153.96, 152.60, 150.73, 145.14, 145.09, 139.06, 132.66, 132.20, 131.81, 129.27, 127.84, 126.22, 126.06, 124.53, 120.96, 119.47, 112.09, 100.99, 60.11, 33.75, 30.80, 25.39, 24.24. HRMS (ESI+): *m*/*z*. 440.23345 [$C_{28}H_{30}N_3O_2$ $(M-KPF_6)^+$, calcd 440.23325].

(ASCP-HE): Compound **2** (100 mg, 0.307 mmol) was added to MeCN (5 mL). 1-bromohexane (507 mg, 3.07 mmol) was then added to the reaction mixture, stirred and refluxed for 24 h. Upon completion of the reaction, the reaction mixture was cooled to room temperature, precipitated with Et_2O, filtered and washed with Et_2O. The precipitate was then redissolved in acetone (10 mL) and saturated KPF_6 aqueous solution (10 mL) and stirred for 1 h. Acetone was then removed and the precipitate was filtered and washed with water to obtain the pure product as a red solid in 47% yield (80.1 mg). ^{1}H NMR (400 MHz, CD_3CN) δ 8.66 (d, *J* = 6.6 Hz, 2H), 8.29 (d, *J* = 6.6 Hz, 2H), 8.02 (d, *J* = 8.5 Hz, 2H), 7.94 (m, 4H), 7.81 (s, 1H), 6.85 (d, *J* = 8.9 Hz, 2H), 4.50 (t, *J* = 7.5 Hz, 1H), 3.09 (s, 6H), 2.01 (m, 2H), 1.45 – 1.29 (m, 6H), 0.93 (t, *J* = 6.7 Hz, 3H). ^{13}C NMR (100 MHz, CD_3CN) δ

155.21, 152.55, 144.65, 144.18, 139.59, 132.55, 131.79, 128.72, 126.16, 124.69, 120.86, 118.91, 111.65, 101.63, 60.93, 39.27, 30.75, 25.26, 22.08, 13.20. HRMS (ESI+): *m*/*z*. 410.25917 [$C_{28}H_{32}N_3$ $(M\text{-}PF_6)^+$, calcd 410.25907].

(ASCP-ES): Compound **2** (100 mg, 0.307 mmol) was added to MeCN (5 mL). ethyl bromoacetate (512 mg, 3.07 mmol) was then added to the reaction mixture, stirred and refluxed for 24 h. Upon completion of the reaction, the reaction mixture was cooled to room temperature, precipitated with Et_2O, filtered and washed with Et_2O. The precipitate was then redissolved in acetone (10 mL) and saturated KPF_6 aqueous solution (10 mL) and stirred for 1 h. Acetone was then removed and the precipitate was filtered and washed with water to obtain the pure product as a red solid in 51% yield (86.8 mg). ^{1}H NMR (400 MHz, DMSO) δ 9.02 (d, *J* = 6.7 Hz, 2H), 8.64 (d, *J* = 6.7 Hz, 2H), 8.21 (d, *J* = 8.5 Hz, 2H), 8.06 (s, 1H), 7.94 (d, *J* = 8.5 Hz, 4H), 6.84 (d, *J* = 9.0 Hz, 2H), 5.60 (s, 2H), 4.25 (q, *J* = 7.1 Hz, 2H), 3.04 (s, 6H), 1.26 (t, *J* = 7.1 Hz, 3H). ^{13}C NMR (100 MHz, DMSO) δ 166.98, 155.00, 152.63, 146.54, 145.24, 139.44, 132.44, 132.25, 129.46, 126.26, 124.21, 120.95, 119.46, 112.10, 100.91, 62.78, 59.89, 40.04, 14.42. HRMS (ESI+): *m*/*z*. 412.20206 [$C_{26}H_{26}N_3O_2$ $(M\text{-}PF_6)^+$, calcd 412.20195].

(ASCP-SO): Compound **2** (100 mg, 0.307 mmol) was added to MeCN (5 mL). 1,3-Propanesultone (375 mg, 3.07 mmol) was then added to the reaction mixture, stirred and refluxed for 24 h. Upon completion of the reaction, the reaction mixture was cooled to room temperature, precipitated with Et_2O, filtered and washed with Et_2O to obtain the pure product as a red solid in 95% yield (131 mg). ^{1}H NMR (500 MHz, DMSO) δ 9.10 (d, *J* = 6.7 Hz, 2H), 8.55 (d, *J* = 6.7 Hz, 2H), 8.19 (d, *J* = 8.6 Hz, 2H), 8.06 (s, 1H), 7.94 (dd, *J* = 10.9, 8.8 Hz, 4H), 6.85 (d, *J* = 9.0 Hz, 2H), 4.71 (t, *J* = 6.7 Hz, 2H), 3.05 (s, 6H), 2.46 (t, *J* = 7.1 Hz, 2H), 2.31 – 2.19 (m, 2H). ^{13}C NMR (125 MHz, DMSO) δ 153.96, 152.59, 145.36, 145.08, 138.98, 132.81, 132.20, 132.02, 129.29, 128.62, 126.21, 126.18, 124.56, 122.80, 121.01, 119.49, 112.10, 101.05, 59.15, 47.43, 27.75. HRMS (ESI+): *m*/*z*. 448.16856 [$C_{25}H_{26}N_3O_3S$ $(M+H)^+$, calcd 448.16894].

(Z)-3-(4-(dimethylamino)phenyl)-2-(pyridin-4-yl)acrylonitrile (1): 4-pyridylacetonitrile hydrochloride (2.00 g, 12.9 mmol) and 4-dimethylaminobenzaldehyde (2.12 g, 14.2 mmol) was added with potassium hydroxide (2.39 g, 42.6 mmol) in 30 mL of ethanol and stirred at room temperature for 4 h. Upon completion of the reaction, 30mL of water was added to the reaction mixture. The yellow precipitates were filtered, washed with water and dried under reduced pressure to yield the product as an orange coloured solid in 92% yield (2.95 g). ^{1}H NMR (400 MHz, $CDCl_3$) δ 8.61 (dd, *J* = 4.9, 1.3 Hz, 1H), 7.91 (d, *J* = 9.0 Hz, 1H), 7.58 (s, 1H), 7.51 (dd, *J* = 4.8, 1.4 Hz, 1H), 6.73 (d, *J* = 9.0 Hz, 1H), 3.09 (s, 3H). ^{13}C NMR (100 MHz, $CDCl_3$) δ 152.37, 150.29, 144.95, 143.06, 132.21, 120.58, 119.29, 118.49, 111.56, 101.10, 40.02. HRMS (ESI+): *m*/*z*. 250.13342 [$C_{16}H_{16}N_3$ $(M+H)^+$, calcd 250.13387].

(ASC): Compound **1** (200 mg, 0.803 mmol) was added to MeCN (10 mL). Iodomethane (171 mg, 1.21 mmol) was then added to the reaction mixture, stirred and refluxed for 24 h. Upon completion of the reaction, the reaction mixture was cooled to room temperature, precipitated with Et_2O, filtered and washed with Et_2O. The precipitate was then redissolved in acetone (20 mL) and saturated KPF_6 aqueous solution (20 mL) and stirred for 1 h. Acetone was then removed and the precipitate was filtered and washed with water to obtain the pure product as a dark blue solid in 71% yield (234 mg). ^{1}H NMR (400 MHz, DMSO) δ 8.80 (d, *J* = 6.9 Hz, 2H), 8.44 (s, 1H), 8.17 (d, *J* = 7.0 Hz, 2H), 8.04 (d, *J* = 9.1 Hz, 2H), 6.91 (d, *J* = 9.1 Hz, 2H), 4.22 (s, 3H), 3.11 (s, 6H). ^{13}C NMR (100 MHz, DMSO) δ 154.32, 151.05, 145.30, 134.44, 121.39, 119.95, 118.41, 112.52, 95.17, 47.08. HRMS (ESI+): *m*/*z*. 264.14933 [$C_{17}H_{18}N_3$ $(M\text{-}PF_6)^+$, calcd 264.14952].

Synthesis Characterization

^{1}H (400MHz or 500MHz) & ^{13}C NMR (100MHz, 125MHz) spectra were acquired on Agilent MR400 or Agilent DD2 instrument. The chemical shift data for each signal are given as δ. High-resolution mass spectra were acquired using a Thermo Scientific Q Exactive Plus Orbitrap LC-MS/MS instrument.

X-ray Diffraction Experiments

X-ray diffraction intensity data for **ASCP** and **ASC** were collected with a Rigaku Synergy Diffractometer using either Cu- Kα or Mo- Kα radiation with the temperature during data collection maintained at 100.0(1)K using an Oxford Cryosystems cooling device. The structure was solved by direct methods and difference Fourier synthesis.[13] Thermal ellipsoid plots were generated using the program ORTEP-3 integrated within the WINGX suite of programs.[14-15] Experimental electrostatic potential data for **ASC** acquired from measured X-ray crystallography data through LS refinement of scale, xyz and Ui,j against high order reflections (d < 0.8Å). Charge density parameters were refined using CGLS against the full dataset (with appropriate constraints and restraints). Charge density parameters were then deconstrained and refined against the full dataset. Scale, xyz and Ui,j parameters were then LS refined against the full dataset until convergence. Visualisation of electrostatic potential were done using MoPro software.[16-18]

Photophysical Characterization

Absorbance and fluorescence spectra were obtained on a Cary 300 UV-Vis spectrometer and Cary Eclipse fluorimeter (Agilent Technologies Inc., Santa Clara, CA, USA), respectively. Data were plotted using Origin 2018 (OriginLab Corp., Northampton, MA, USA). Absolute photoluminescence quantum yield measurements were acquired by using an integrating sphere (F3018, Horiba Jobin Yvon) on a Jobin Yvon FluorologOR-3 fluorimeter. All spectra for the absolute quantum yield measurements were corrected for the light source noise, wavelength sensitivity and the transmittance of filters. 488 nm excitation wavelength was used for all measurements. 2 mM dye concentration in 2 wt% PMMA acetone solutions were spin-coated on glass substrate (600 rpm, 1min) for dye-PMMA film fabrication.

DFT Calculations

DFT calculations were carried out using B3LYP/ 6-31g* on Gaussian16 for all calculations. Visualisation of structures were done using Avogadro 1.20[19] and GaussView 5.0. No negative frequencies for optimised structures were observed.

Cell Culture

A549 cells were cultured in DMEM (Life Technologies, Catalog Number: 11965118) supplemented with 10% fetal bovine serum at 37ºC in 5% CO2 air with humidification.

Cell Viability Assay

2×10^4 cells were plated onto 96-well plates 24hr prior to dye application. CLARIOstar monochromator plate reader (BMG Labtech) in fluorescence intensity mode with excitation at 560/15nm and emission at 590/20nm was used to assess cell viability using Alamar Blue assay (Catalog number: DAL1025, Thermo Fisher Scientific).

Cell Staining

All dyes were dissolved in DMSO as 5 mM, **ASCP-SO** was dissolved in DMSO as 2 mM stock. Stock solution of dyes were kept at 4 ºC in the dark. A549 cells (1.5×10^4) were plated either on an ibidi µ-Slide 8 Well, ibiTreat (ibidi, Catalog number: 80826-90) for fixed cell imaging 15 mm glass bottom culture dishes (Nest, Catalog number: 801002) for live cell imaging. Plated cells were treated with freshly diluted dye for 30min at 37ºC and subsequently washed. For fixed cell imaging, cells were fixed on plate with

4% (w/v) paraformaldehyde (PFA) in PBS for 15min at room temperature. For live cell imaging, cells were imaged at 37ºC and 5% CO_2 air.

Confocal Laser Scanning Microscopy

After staining, cells were fixed with 4% (w/v) paraformaldehyde in PBS for 15min at room temperature. For live cell imaging, cells were imaged at 37 ºC and 5% CO_2 air. Images were acquired on a Zeiss LSM 780 microscope using a 63× objective lens. For image acquisition, the pixel frame size was set at 1024×1024 or 512×512 and the pixel dwell time was 25.4 µs or 50.4 µs. For **ASCP** and derivatives (excitation: 488 nm; emission: 615 – 650 nm), **ASC** (excitation: 488 nm; emission 520 – 560 nm) and Mitotracker™ Deep Red (excitation: 633 nm; emission 660 – 700nm).

Acknowledgements

We thank LIMS Bioimaging Platform, La Trobe University for the access to the confocal microscope. We thank the Bio21 Mass Spectromoetry and Proteomics Facility for technical support and access to mass spectrometers. This work was supported by grants to Y.H. (Australian Research Council DE170100058, Rebecca L. Cooper Medical Research Foundation PG2018043, and Australia-China Science and Research Fund-Joint Research Centre for Personal Health Technologies ACSRF65777) and WWHW (Australian Research Council CE170100026).

Keywords: Molecular rotor • aggregation induced emission • mitochondria dyes • fluorescent probes • cell imaging

[1] R. O. Loutfy, B. A. Arnold, *J. Phys. Chem.* **1982**, *86*, 4205-4211.
[2] J. Sutharsan, D. Lichlyter, N. E. Wright, M. Dakanali, M. A. Haidekker, E. A. Theodorakis, *Tetrahedron.* **2010**, *66*, 2582-2588.
[3] Z. Yang, J. Cao, Y. He, J. H. Yang, T. Kim, X. Peng, J. S. Kim, *Chem. Soc. Rev.* **2014**, *43*, 4563-4601.
[4] Y. Hong, J. W. Y. Lam, B. Z. Tang, *Chem. Commun.* **2009**, 4332-4353.
[5] Y. Hong, J. W. Y. Lam, B. Z. Tang, *Chem. Soc. Rev.* **2011**, *40*, 5361-5388.
[6] C. Y. Y. Yu, W. Zhang, R. T. K. Kwok, C. W. T. Leung, J. W. Y. Lam, B. Z. Tang, *J. Mater. Chem. B.* **2016**, *4*, 2614-2619.
[7] Y.-L. P. Ow, D. R. Green, Z. Hao, T. W. Mak, *Nat. Rev. Mol. Cell Biol.* **2008,** *9*, 532-542.
[8] D. E. Handy, J. Loscalzo, *Antioxid. Redox Sign.* **2011**, *16*, 1323-1367.
[9] G. Barshad, S. Marom, T. Cohen, D. Mishmar, *Trends Genet.* **2018**, *34*, 682-692.
[10] C. Wang, R. J. Youle, *Annu. Rev. Genet.* **2009**, *43*, 95-118.
[11] M. Filosto, M. Scarpelli, M. S. Cotelli, V. Vielmi, A. Todeschini, V. Gregorelli, P. Tonin, G. Tomelleri, A. Padovani, *J. Neurol.* **2011**, *258*, 1763-1774.
[12] Johri, M. F. Beal, *J. Pharmacol. Exp. Ther.* **2012**, *342*, 619.
[13] G. M. Sheldrick, *Acta Crystallogr. C* **2015**, *71*, 3-8.
[14] L. J. Farrugia, *J. Appl. Crystallogr.* **1997**, *30*, 565-565.
[15] L. J. Farrugia, *J. Appl. Crystallogr.* **1999**, *32*, 837-838.
[16] B. Fournier, B. Guillot, C. Lecomte, E. C. Escudero-Adán, C. Jelsch, *Acta Crystallogr. A* **2018**, *74*, 170-183.
[17] Nassour, S. Domagala, B Guillot, T. Leduc, C. Lecomte, C. Jelsch, *Acta Crystallogr. B* **2017**, *73*, 610-625.
[18] A. Jelsch, B. Guillot, A. Lagoutte, C. Lecomte, *J. Appl. Crystallogr.* **2005**, *38*, 38-54.
[19] M. D. Hanwell, D. E. Curtis, D. C. Lonie, T. Vandermeersch, E. Zurek, G. R. Hutchison, *J. Cheminformatics* **2012**, *4*, 17.

Entry for the Table of Contents

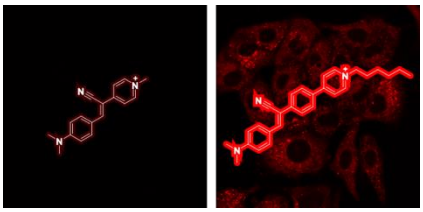

AIE-active molecular rotors for mitochondria imaging with improved uptake and retention in both live and fixed cells.

Institute and/or researcher Twitter usernames: @yuning_hong, @wallacexwong, @excitonscience, @SciMelb, @Bio21Institute, @LIMSLTU, @LTUresearchers